

FCDM: A Physics-Guided Bidirectional Frequency Aware Convolution and Diffusion-Based Model for Sinogram Inpainting

Jiaze E¹, Srutarshi Banerjee², Tekin Bicer², Guannan Wang¹, Yanfu Zhang¹, Bin Ren¹

¹Department of Computer Science, William & Mary, USA

²Argonne National Laboratory, USA

je@wm.edu, sruban@anl.gov, tbicer@anl.gov, gwang01@wm.edu, yzhang105@wm.edu, bren@wm.edu

Abstract

Computed tomography (CT) is widely used in scientific and medical imaging, but acquiring full-view sinograms requires high radiation dose and long scan times. Sparse-view CT alleviates this burden but yields incomplete sinograms with structured signal loss, hampering accurate reconstruction. Unlike RGB images, sinograms encode overlapping features along projection paths and exhibit directional spectral patterns. Standard inpainting models overlook these properties, treating missing data as local holes and neglecting angular dependencies and physical consistency. We propose FCDM, a diffusion-based framework tailored for sinograms, which restores global structure through bidirectional frequency reasoning and angular-aware masking, while enforcing physical plausibility via physics-guided constraints and frequency-adaptive noise control. Experiments on synthetic and real-world datasets show that FCDM consistently outperforms baselines, achieving SSIM over 0.93 and PSNR above 31 dB across diverse sparse-view scenarios.

1 Introduction

X-ray computed tomography (XCT) is a vital 3D imaging technique widely used in synchrotron facilities for high-resolution internal structure analysis. XCT generates *parallel beam* projections by rotating a sample under collimated X-rays. These projections are organized into a 3D dataset and sliced row-by-row, producing *sinograms* that are then reconstructed into 3D images via computationally intensive algorithms (Chen et al. 2019; Hidayetoğlu et al. 2019; Bicer et al. 2017). For instance, the nano-CT beamlines at the Advanced Photon Source at Argonne National Laboratory offer cutting-edge imaging capabilities, achieving sub-20 nm spatial resolution (De Andrade et al. 2016). These capabilities enable critical studies in battery defect analysis (Zhao et al. 2024; Müller et al. 2018), neurodegenerative disease research (Koroshetz et al. 2018; Dyer et al. 2017; Hidayetoğlu et al. 2020), and materials science (Satapathy et al. 2024). While XCT provides high-precision imaging, its high radiation dose can degrade samples, increase scanning time, and raise computational costs (Brenner and Hall 2007). These challenges are particularly pronounced when imaging fragile biological or reactive materials.

Copyright © 2026, Association for the Advancement of Artificial Intelligence (www.aaai.org). All rights reserved.

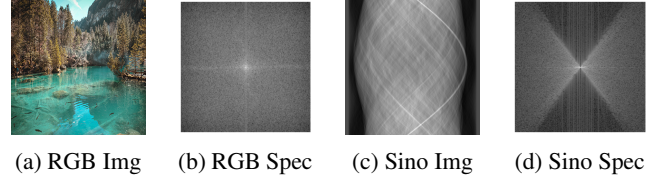


Figure 1: **Comparisons of RGB and sinogram and their spectra.** Unlike RGB images, which have localized frequency components, sinograms exhibit structured spectral distributions due to the Radon transform.

To alleviate these limitations, sparse-view CT reduces the number of projections, thereby lowering radiation exposure and acquisition time. However, this comes at the cost of severely incomplete sinograms, which compromise reconstruction quality and introduce artifacts and structural loss. These issues cannot be resolved by simply acquiring denser views, which may be infeasible due to sample fragility or experimental constraints, nor by correcting reconstructed images, as missing sinogram data leads to nonlinear reconstruction distortions, where early-stage errors propagate and amplify, making it impossible to recover post hoc. As a result, effective sinogram inpainting becomes essential.

Most existing inpainting models are designed for RGB images, where each pixel corresponds to a localized structure. In contrast, sinograms encode integrated X-ray projections, exhibiting global feature entanglement. The fundamental differences render traditional spatial-domain methods inadequate. To address this, we build a sinogram-specific inpainting framework FCDM that systematically accounts for these challenges through four targeted designs.

One key limitation of conventional spatial-domain inpainting models (Liu et al. 2024; Zhang et al. 2023; Ko and Kim 2023; Deng et al. 2022; Lugmayr et al. 2022; Li et al. 2022; Suvorov et al. 2022) is their inability to handle feature entanglement (Defrise and Clack 1994) in sinograms. Unlike RGB images, where each pixel corresponds to a localized structure, sinogram pixels encode integrals along X-ray paths, mixing contributions from multiple spatial regions. This projection-overlap causes missing areas to reflect non-local ambiguities that spatial context alone cannot resolve. Although both RGB images and sinograms ex-

hibit frequency-based structure, sinograms differ fundamentally in that their two axes—detector position and projection angle—represent physically distinct variables. This asymmetry, introduced by the Radon transform (Radon 1917), leads to highly organized and directional spectral patterns (see Fig. 1), allowing overlapping structures to be more distinctly separated in frequency space than in spatial domain. These properties make frequency-based decomposition especially suitable. To this end, we propose bidirectional frequency-domain convolutions (BFDC), which independently process frequency features along detector and angle axes. Unlike spatial convolutions that ignore projection geometry, or 2D frequency convolutions that treat both axes equally, BFDC enables axis-aware decomposition. Applying a joint 2D frequency convolution would treat the two axes as equivalent—which is reasonable for RGB images, but in sinograms, the detector and angle axes correspond to fundamentally different physical meanings. Our bidirectional approach also allows for assigning distinct weights along each axis, enabling targeted feature extraction and dynamic balance between local fidelity and global consistency.

Another key limitation of existing methods is their failure to enforce physical consistency, particularly total absorption conservation (Kak and Slaney 2001)—a fundamental principle in X-ray imaging which requires that the sum of attenuation values along each projection remains stable across the scan. While critical for accurate reconstruction, this constraint is largely overlooked in deep learning-based inpainting models, which typically treat sinograms as generic 2D images and optimize for pixel-wise similarity. To address this, we introduce a physics-guided loss function that enforces total absorption consistency, encouraging the network to preserve the integral structure along projection paths. In addition, we incorporate a frequency-domain regularization term to stabilize spectral behavior, ensuring that the restored sinograms adhere to both physical constraints and expected spectral behavior, thereby preventing frequency inconsistencies that propagate as artifacts during reconstruction.

Further, standard diffusion models use binary 0/1 masks, which work well for RGB images where missing pixels are spatially localized and independent. However, in sinograms, each structure appears across multiple projection angles, causing missing regions to be highly correlated and angularly distributed. A plain 0/1 mask lacks angular context, providing no information about which projection angle a missing value belongs to. This makes it difficult for the model to align missing data with observed patterns from other angles during denoising. To address this, we introduce Fourier-enhanced mask embedding (FEME), which encodes the projection angle of each missing region into the mask representation. This enables the model to interpret mask locations not just spatially but angularly, allowing it to leverage observed structures from other views and improve the consistency and physical plausibility of the sinogram.

Finally, standard diffusion models apply uniform Gaussian noise across all frequency components, which may suffice for RGB images but fails to reflect the reconstruction sensitivity of sinogram data. While both image types associate low-frequency with global structure and high-

frequency with detail, sinograms are more vulnerable to early low-frequency perturbations: due to the integral nature of the inverse Radon transform, such errors can accumulate and propagate globally—manifesting as ringing artifacts, brightness drift, or structural distortion—and severely corrupt the final reconstruction (Würfl et al. 2016). To address this, we propose frequency-adaptive noise scheduling (FANS), which preserves low-frequency components during early denoising to stabilize global structure inpainting to promote stable global recovery, and gradually shifts emphasis to high-frequency details as denoising progresses.

In summary, our key contributions are:

- We propose FCDM, a physics-guided, frequency-aware diffusion framework specifically designed for sinogram inpainting, tackling both feature entanglement and physical constraint violations overlooked by prior methods.
- We introduce BFDC that separately extract spectral features along projection and detector dimensions, enabling structured frequency disentanglement. We further design a physics-informed loss that enforces total absorption consistency and spectral stability.
- We enhance diffusion-based inpainting robustness via FEME that encodes angular context into missing regions, and FANS that aligns denoising progression with sinogram recovery dynamics.
- Extensive experiments on one real-world dataset (De Carlo et al. 2018) and two synthetic datasets show that FCDM consistently achieves over 0.93 SSIM (Wang et al. 2004) and 31 dB PSNR, with ablation results confirming the contribution of each module.

2 Related Work

Deep learning-based methods have shown great promise in RGB image inpainting. (Zhang et al. 2023) proposes a joint optimization method based on a Bayesian framework. (Ko and Kim 2023) applies a continuous mask on Transformer-based structure. (Deng et al. 2022) proposes a new Hourglass attention structure and combines it with the Transformer structure. (Li et al. 2022) presents a new inpainting framework with multi-level interactive siamese filtering using an interactive dynamic kernel prediction mechanism. (Suvorov et al. 2022) proposes LaMa which utilizes fast Fourier convolution (Chi, Jiang, and Mu 2020a) to solve large masking problems. (Lugmayr et al. 2022) proposes an inpainting method that solely leverages an off-the-shelf unconditionally trained denoising diffusion probabilistic models (DDPM). (Liu et al. 2024) uses diffusion-based structure guidance to solve the problem of semantic discrepancy in masked and unmasked regions. However, RGB image inpainting methods do not consider the unique physical constraints and feature entanglements in sinograms.

Traditional mathematical methods have also been employed for sinogram inpainting. Linear (Herman and Meyer 1993) and spline interpolation (Unser 1999) estimate the missing sinogram data based on the known data. Total Variation (TV) minimization (Chambolle and Lions 1997), originally developed for image denoising and reconstruction, has

also been applied to sinogram inpainting. It works by promoting sparsity in the gradient domain, making it effective for inpainting sinograms with small missing regions. While these mathematical methods provide simple and interpretable solutions, they struggle with large missing regions.

Recently, several deep learning-based models have been proposed for sinogram inpainting. (Yao et al. 2024; Zhao et al. 2018) utilize U-Net to directly interpolate missing sinogram data. (Valat, Farrahi, and Blumensath 2023a; Li et al. 2019a; Valat, Farrahi, and Blumensath 2023b; Xie et al. 2022) employ GANs to generate realistic sinogram patches. (Jiaze et al. 2025) uses Transformer blocks to inpaint geometric shapes sinograms. However, these methods typically operate in the spatial domain and may struggle to enforce global consistency or preserve underlying frequency characteristics. Other deep learning-based models apply unique characteristics of sinograms. (Li et al. 2019b,c) incorporate periodicity into the loss function to leverage the cyclical nature of certain sinograms. (Wagner et al. 2023; Li et al. 2019a) compare the reconstructed images from the inpainted and ground truth sinograms in their loss calculations. (Sun et al. 2021) combines coordinate mapping and Fourier feature mapping together with multilayer perceptron to help the inpainting. While these strategies improve inpainting fidelity to some extent, they generally lack explicit modeling of sinogram behavior in the frequency domain and do not directly regulate the progression of the inpainting process. Several recent approaches take a different direction by bypassing sinogram inpainting entirely and instead reconstructing images directly from incomplete sinograms using deep generative models. Representative works include (Liu et al. 2023; Hu et al. 2023; Guo, Lopez-Tapia, and Katsaggelos 2025), which refine reconstructed images through learned priors or image-space denoising. While effective in mitigating image artifacts, these methods forgo direct control over sinogram consistency, making it difficult to correct upstream projection-domain distortions.

3 FCDDM Design and Analysis

FCDDM is a two-stage framework designed for sinogram inpainting, combining an encoder-decoder network with a diffusion-based restoration process. As illustrated in Fig. 2, stage 1 focuses on representation learning, while stage 2 performs guided denoising for inpainting. In stage 1, the model learns a latent representation of the input sinogram. Specifically, an encoder maps the sinogram into a latent space, which is then processed using BFDC to extract spatial and frequency-domain features across projection angles and detector positions. These enriched features are decoded to recover the sinogram. The encoder-decoder is trained with pixel-wise and adversarial losses, augmented by two custom losses that promote frequency consistency and physical realism. After training, its parameters are frozen to ensure consistent feature extraction in the next phase. In stage 2, a diffusion-based model (Ho, Jain, and Abbeel 2020) is trained to perform inpainting on the latent representations. During training, random binary masks are applied to simulate missing or corrupted sinogram regions across various angular spans. The mask information is embedded into

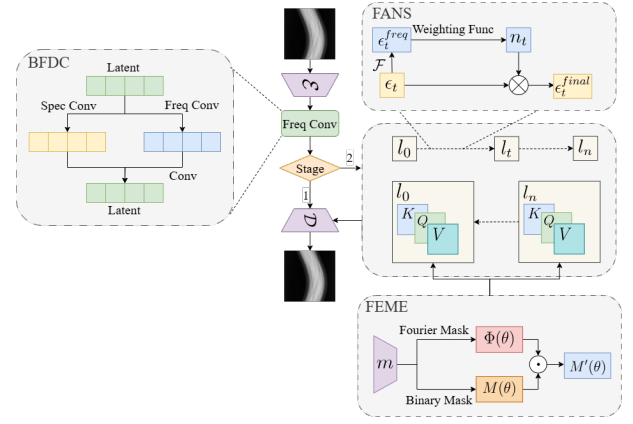


Figure 2: **Overview of FCDDM**. Stage 1 trains an encoder-decoder network equipped with BFDC. In stage 2, a diffusion-based model performs inpainting within the encoded latent, guided by FEME and FANS. The final output is obtained by decoding the inpainted latent. l represents latent obtained from the encoder. m represents mask. K , Q , V represent the query, key, and value matrices from the attention mechanism.

the model via a Transformer-style attention mechanism, enabling the diffusion process to be conditionally guided. To enhance the diffusion process, we introduce FEME, which encodes the angular context of missing regions into the mask embedding, improving geometric awareness. Additionally, we propose FANS, a frequency-adaptive noise scheduling strategy that preserves low-frequency components during early denoising to stabilize global structure, and progressively emphasizes high-frequency components in later steps to refine fine details.

3.1 Bidirectional Frequency-Domain Convolutions

To enhance feature extraction in the latent space, we introduce bidirectional frequency-domain convolutions (BFDC). Given a sinogram input $s \in \mathbb{R}^{C \times H \times W}$, the encoder $\mathcal{E}(\cdot)$ maps it to a latent representation $h = \mathcal{E}(s)$, $h \in \mathbb{R}^{C' \times H' \times W'}$. We then apply both spatial and frequency-domain convolutions to h . A standard spatial convolution $\mathcal{G}(\cdot)$ produces a spatial representation $h_s = \mathcal{G}(h)$. We also perform frequency-domain convolutions along two orthogonal dimensions—detector (W') and projection angle (H')—to capture directional spectral features that are entangled in the sinogram.

Specifically, we apply real-valued Fourier transforms (RFFT) (Cooley and Tukey 1965) along the width and height axes of h , yielding complex-valued representations \hat{h}_w and \hat{h}_h . These are multiplied with corresponding frequency-domain kernels \mathcal{K}_w and \mathcal{K}_h via Hadamard product, then transformed back to the spatial domain using an inverse RFFT to obtain frequency-enhanced features:

$$y_w = \mathcal{F}_w^{-1}(\mathcal{K}_w \cdot \mathcal{F}_w(h)), \quad y_h = \mathcal{F}_h^{-1}(\mathcal{K}_h \cdot \mathcal{F}_h(h)). \quad (1)$$

Unlike full 2D Fourier convolutions, which treat the two axes equally and may obscure their distinct physical meanings, our directional decomposition allows independent processing of features along projection and detector axes. The final representation is computed as a weighted fusion of the spatial and frequency-enhanced components:

$$y = \alpha_s h_s + \alpha_w y_w + \alpha_h y_h, \quad (2)$$

where α_s , α_w , and α_h are weighting factors that ensure spatial-domain information and frequency-domain information along both projection angles and detector positions are optimally integrated. The fused representation y is then decoded by the decoder $\mathcal{D}(\cdot)$ to produce the reconstructed sinogram $\bar{s} = \mathcal{D}(y)$.

3.2 Physics-Guided Loss Functions

Total Projection Consistency Loss In CT, the total X-ray absorption along each projection should remain consistent with the object’s integral attenuation. This ensures that no non-physical intensity drift is introduced, which could distort the sinogram inpainting and further the final CT reconstruction. To enforce this constraint, we require the sum of all projection values to match the total absorption of the projection data:

$$\sum_{\theta} \sum_s P_{\theta}(s) = \int \mu(x, y) dx dy. \quad (3)$$

Here, $P_{\theta}(s)$ is the measured projection at angle θ and detector position s , and $\mu(x, y)$ is the object’s attenuation coefficient. Since $\mu(x, y)$ is not directly available during training, we approximate the total absorption via the inverse Radon transform $\mathcal{R}^{-1}\{P_{\theta}(s)\}$, and define the following loss:

$$\mathcal{L}_{\text{absorp}} = \left(\sum_{\theta} \sum_s P_{\theta}(s) - \int \mathcal{R}^{-1}\{P_{\theta}(s)\} dx dy \right)^2. \quad (4)$$

This term penalizes global mismatches between the measured projections and their corresponding inferred attenuation distribution, encouraging physically consistent inpainting.

Frequency Domain Consistency Loss Since sinogram information is naturally structured in the frequency domain, ensuring spectral consistency between inpainted and ground-truth sinograms is essential. We define this constraint by minimizing the L2 norm of the frequency difference between the inpainted and ground-truth sinograms:

$$\mathcal{L}_{\text{freq}} = \sum_u \sum_v \{ \mathcal{F}(\bar{\mu}(x, y)) - \mathcal{F}(\mu(x, y)) \}^2. \quad (5)$$

where \mathcal{F} denotes the 2D Fourier transform. This loss ensures that the model accurately captures the structural characteristics of sinograms in the frequency domain, preventing spectral artifacts.

Overall Loss The final loss for stage 1 training combines pixel-wise reconstruction, adversarial learning, and physics-guided constraints:

$$\mathcal{L}_1 = \lambda_{\text{pixel}} \mathcal{L}_{\text{pixel}} + \lambda_{\text{adv}} \mathcal{L}_{\text{adv}} + \lambda_{\text{absorp}} \mathcal{L}_{\text{absorp}} + \lambda_{\text{freq}} \mathcal{L}_{\text{freq}}. \quad (6)$$

where $\mathcal{L}_{\text{pixel}}$ ensures pixel-wise reconstruction accuracy, and \mathcal{L}_{adv} is the adversarial loss. In stage 2, the diffusion model optimizes a mean squared error (MSE) loss.

3.3 Fourier-Enhanced Mask Embedding

Standard diffusion-based inpainting methods use binary 0/1 masks to indicate missing regions. Unlike RGB images, sinograms exhibit global feature entanglement due to the projection process. The same physical structure may appear at different spatial positions across projection angles, while a simple binary mask offers no indication of these angular correlations. As a result, the model may interpret missing areas as independent holes, failing to capture their underlying coherence. To address this, we introduce Fourier-Enhanced Mask Embedding (FEME), which augments each mask entry with direction-aware features to better reflect the sinogram’s projection geometry. Instead of treating projection angles as raw scalar inputs, we encode each angle using a Fourier basis, capturing the periodic nature of angular variation. Given a projection angle θ , we compute its Fourier representation as

$$\Phi(\theta) = [\sin(2\pi f_1 \theta), \cos(2\pi f_1 \theta), \dots, \cos(2\pi f_N \theta)], \quad (7)$$

where f_i represents a set of predefined frequencies. This encoding transforms scalar angles into a structured representation that preserves their cyclical relationships and enhances expressiveness. The encoded angle is broadcast to each detector position and concatenated with the binary mask $M(\theta)$, which is expanded from a scalar to a vector to match the dimension:

$$M'(\theta) = [M(\theta); \Phi(\theta)]. \quad (8)$$

This operation enriches the original binary mask with projection-specific context. By embedding angular information in a periodic, high-dimensional form, FEME enables the model to better identify structural correspondences across projections, leading to more coherent and physically consistent inpainting results.

3.4 Frequency-Adaptive Noise Scheduling

In standard diffusion models, Gaussian noise is injected uniformly across all frequency components, ignoring the structural characteristics of the data. Low-frequency components encode global structure, whereas high-frequency components capture fine details, playing distinct roles during denoising. Moreover, due to the Radon transform, sinogram frequencies exhibit directional coupling, and disrupting specific bands can lead to global artifacts such as distortion or ringing in the final reconstruction. To address this, we propose frequency-adaptive noise scheduling (FANS), which adjusts the spectral distribution of noise over the course of diffusion. Specifically, FANS preserves low-frequency components during early denoising steps to stabilize global structure recovery, and gradually shifts focus to high-frequency perturbations as finer details are restored.

The process begins by generating standard Gaussian noise $\epsilon_t \sim \mathcal{N}(0, I)$, followed by a two-dimensional Fourier transform to obtain its frequency representation $\epsilon_t^{\text{freq}} = \mathcal{F}(\epsilon_t)$.

Methods	SSIM			PSNR		
	Mask Ratio			Mask Ratio		
	0.4	0.6	0.8	0.4	0.6	0.8
Ours	0.937 (0.915)	0.938 (0.918)	0.940 (0.919)	31.0 (29.2)	31.1 (29.4)	31.3 (29.3)
RePaint	0.922 (0.901)	0.928 (0.905)	0.926 (0.902)	29.8 (27.3)	30.0 (27.5)	29.9 (27.6)
CoPaint	0.915 (0.891)	0.918 (0.895)	0.919 (0.894)	29.0 (27.0)	29.2 (27.2)	29.4 (27.1)
MISF	0.909 (0.880)	0.911 (0.883)	0.908 (0.882)	29.1 (27.0)	29.2 (27.2)	29.0 (27.1)
LaMa	0.900 (0.870)	0.899 (0.869)	0.901 (0.871)	28.9 (26.7)	28.8 (26.9)	28.7 (26.8)
StrDiffusion	0.840 (0.801)	0.838 (0.805)	0.841 (0.804)	27.2 (24.6)	27.1 (24.8)	27.0 (24.7)
SionTx	0.826 (0.785)	0.828 (0.789)	0.822 (0.790)	27.1 (24.2)	26.9 (24.4)	26.8 (24.5)
Hourglass	0.785 (0.747)	0.792 (0.748)	0.788 (0.745)	25.5 (23.1)	25.6 (23.3)	25.4 (23.2)
UsiNet	0.630 (0.598)	0.635 (0.601)	0.622 (0.589)	22.1 (19.5)	21.8 (19.8)	21.5 (19.2)
CoIL	0.737 (0.701)	0.739 (0.699)	0.734 (0.695)	23.9 (21.4)	23.7 (21.6)	23.5 (21.3)
CMT	0.715 (0.673)	0.711 (0.671)	0.709 (0.668)	23.1 (20.5)	23.0 (20.6)	22.8 (20.3)

Table 1: **Quantitative accuracy results on the Real-world dataset.** The values in parentheses correspond to the results of the reconstructed images. The comparisons of Shape and Shepp2d datasets are in appendix.

We then apply a time-dependent weighting function $n_t(u, v)$ to modulate the spectral content:

$$n_t(u, v) = 1 + \alpha \left(1 - \frac{t}{T}\right) \cdot \text{dist}(u, v) + \beta \frac{t}{T} \cdot (1 - \text{dist}(u, v)), \quad (9)$$

where $\text{dist}(u, v) = \frac{\sqrt{u^2 + v^2}}{d_{\max}}$ represents the normalized distance to the low-frequency origin, and $d_{\max} = \sqrt{(H/2)^2 + (W/2)^2}$ denotes the maximum frequency magnitude. The parameters α and β control the relative contribution of high-frequency and low-frequency perturbations, respectively. T is the total number of diffusion steps, and t denotes the current step.

The weighted noise is computed via element-wise multiplication and then transformed back to the spatial domain:

$$\epsilon_t^{\text{adapted}} = \mathcal{F}^{-1}(n_t \cdot \epsilon_t^{\text{freq}}). \quad (10)$$

Although FANS improves the spectral targeting of noise, it may still disturb global consistency, particularly in terms of total attenuation along projection paths. To mitigate this, we introduce a soft absorption constraint that penalizes deviations in row-wise intensity while avoiding rigid enforcement that could hurt generalization. While global zero-mean noise is sufficient for natural images, sinograms require row-wise consistency due to the physical meaning of each projection. Therefore, we correct each row’s mean to reduce bias in total attenuation. Specifically, we compute the row-wise sum of the adapted noise and apply a normalization term. Let $N[i] = \sum_j \epsilon_t^{\text{adapted}}[i, j]$ where W is the width of the sinogram. The final correction is given by:

$$\epsilon_t^{\text{final}} = \epsilon_t^{\text{adapted}} - \lambda \frac{N}{W}, \quad (11)$$

where the subtraction is applied row-wise: each element in row i is reduced by $\frac{N_i}{W}$. $\lambda = 1$ enforces full projection consistency, $\lambda = 0$ disables correction, and values between offer a balance between physical plausibility and generalization.

The final adjusted noise is injected into the denoising process using the standard diffusion update:

$$x_t = \sqrt{1 - \beta_t} x_{t-1} + \sqrt{\beta_t} \epsilon_t^{\text{final}}. \quad (12)$$

4 Evaluation

This section evaluates FCDM on 3 datasets: Real-world (De Carlo et al. 2018), Shapes generated using (Van der Walt et al. 2014), and Shepp2d generated using (Gürsoy et al. 2014), and compares it with 10 baselines, including UsiNet (Yao et al. 2024), SionTx (Jiaze et al. 2025), CoIL (Sun et al. 2021), StrDiffusion (Liu et al. 2024), CoPaint (Zhang et al. 2023), CMT (Ko and Kim 2023), Hourglass (Deng et al. 2022), RePaint (Lugmayr et al. 2022), MISF (Li et al. 2022), and LaMa (Suvorov et al. 2022).

The evaluation has three main objectives: (1) demonstrating that FCDM outperforms all baselines, particularly on complex real-world datasets (4.2); (2) conducting ablation studies to validate the effectiveness of our four key designs, including BFDC, physics-guided loss function, FEME, and FANS (4.3).

4.1 Experimental Setup

Implementation Details We train our model using the Polaris supercomputer at Argonne Leadership Computing Facility (ALCF) resources at Argonne National Laboratory (ANL). Polaris supercomputer consists of 560 compute nodes, each of which is equipped with 4 NVIDIA A100 GPUs (connected via NVLink). All training is conducted on a single A100 GPU within one compute node. We use PyTorch version 2.1.0 and CUDA version 12.2. We adopt a two-stage training strategy. In the first stage, we initialize the encoder-decoder using pretrained weights provided by the official latent diffusion models (Rombach et al. 2022) GitHub repository, and fine-tune it on our dataset. In the second stage, we freeze the autoencoder and train the diffusion module using our dataset. For baseline methods, we use the official implementations from GitHub released by the original authors and fine-tune them on our dataset. All models are evaluated under the same resolution (512×512), and input normalization to ensure fairness. For BFDC, α_s , α_h , and α_w are adjusted to 1.0, 0.55 and 0.45, respectively, as sinograms exhibit smoother variations along the projection angle direction (H) but more complex frequency distributions along the detector axis (W) (Li et al. 2020). The loss function is a weighted combination of several components with the following coefficient: pixel loss $\alpha_{\text{pixel}} = 1.0$,

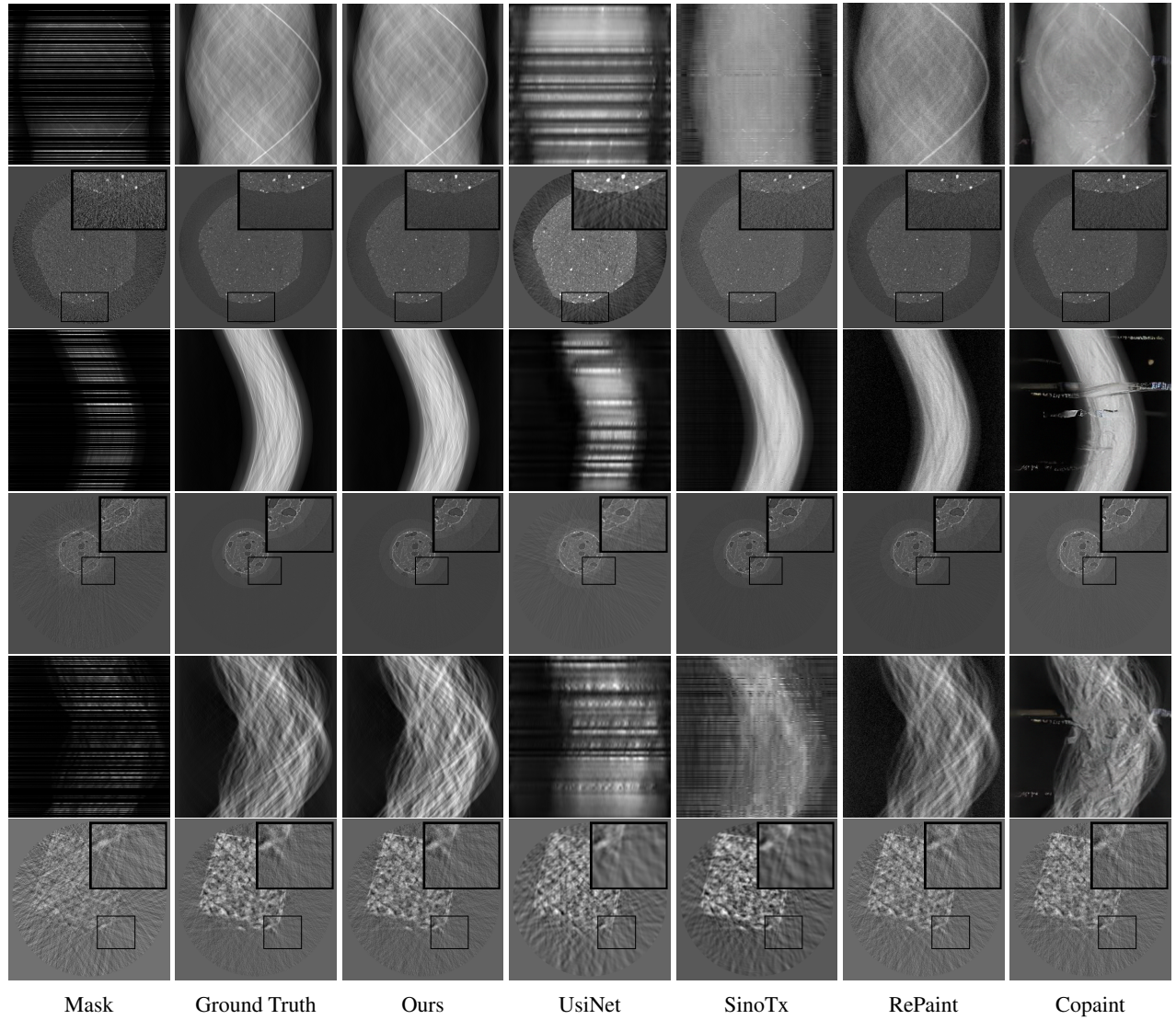


Figure 3: **Visual results of the Real-world dataset.** Lines 1, 3, 5 show visual results of sinogram inpainting and lines 2, 4, 6 show the reconstructed images of the sinograms. Details for Shapes and Shepp2d datasets are in appendix.

adversarial loss $\alpha_{adv} = 0.05$, absorption consistency loss $\alpha_{absorp_sum} = 0.1$, and frequency domain loss $\alpha_{freq} = 0.1$. For FEME, we set the Fourier encoding frequencies as $f_i = i$ with $N = 4$. This provides sufficient angular resolution while avoiding redundancy or overfitting in the mask embedding. For FANS, we set $\alpha = 1.1$ and $\beta = 0.8$ to gently reweight the spectral noise distribution, introducing a mild bias toward high-frequency variation without disrupting low-frequency continuity. The soft absorption constraint is controlled by $\lambda = 0.3$, allowing limited variations in total absorption to improve generalization. During training, the mask ratio is randomly chosen within a range from 0.1 to 0.9 with the corresponding proportion of angles being randomly masked. The learning rate is adjusted based on the formula: $lr = lr_{base} \times batch\ size \times GPU\ num \times grad\ accum\ steps$. All reported quantitative results are averaged over 3 inde-

pendent runs. More details are in appendix.

Dataset Three datasets are used in our experiments, each containing 100k samples for training and 100 samples for testing, with a resolution of 512×512 . Real-world dataset (De Carlo et al. 2018) consists of real sinogram images obtained from various materials and objects, derived from actual synchrotron radiation CT experiments, including Advanced Photon Source (APS) at ANL. Shape dataset generated using the scikit-image library (Van der Walt et al. 2014) contains a variety of simulated geometric shapes. Shepp2d dataset generated by the Tomopy library (Gürsoy et al. 2014) comprises simulated shepp-logan phantoms. More details are in appendix.

Metrics We evaluate inpainting quality using Structural Similarity Index Measure (SSIM) and Peak Signal-to-Noise

Methods	SSIM			PSNR		
	Mask Ratio			Mask Ratio		
	0.4	0.6	0.8	0.4	0.6	0.8
Ours	0.937	0.938	0.940	31.0	31.1	31.3
2D Freq Conv	0.912	0.915	0.916	28.9	29.1	29.2
W/o W Conv	0.906	0.911	0.912	28.6	28.7	28.9
W/o H Conv	0.901	0.906	0.905	28.1	28.3	28.4
Spatial Conv	0.888	0.892	0.890	27.7	27.9	28.0
W/o Freq Conv	0.880	0.885	0.882	27.4	27.7	27.6

Table 2: **Ablation results on frequency-domain convolutions.** The experimental results show that FCDM’s performance is greatly impacted by the frequency domain convolution. Furthermore, there is a marginally more noticeable drop in performance when the H dimension convolution is absent than when the W dimension convolution is absent.

Methods	SSIM			PSNR		
	Mask Ratio			Mask Ratio		
	0.4	0.6	0.8	0.4	0.6	0.8
Ours	0.937	0.938	0.940	31.0	31.1	31.3
W/o \mathcal{L}_{adv}	0.921	0.922	0.924	29.3	29.5	29.6
W/o \mathcal{L}_{freq}	0.917	0.918	0.919	29.0	29.1	29.3
W/o \mathcal{L}_{absorp_sum}	0.909	0.910	0.912	28.5	28.6	28.8

Table 3: **Ablation results on tailored loss.** The results illustrate FCDM’s performance on Real-world when specific terms are removed from the loss function. It is evident that the model’s performance degrades when either \mathcal{L}_{absorp_sum} or \mathcal{L}_{freq} is excluded.

Ratio (PSNR). SSIM quantifies structural preservation by measuring differences in structure, luminance, and contrast. PSNR assesses reconstruction fidelity by comparing signal strength to noise levels. These metrics are chosen for their effectiveness in evaluating both structural accuracy and artifact reduction. More details are in appendix.

4.2 Accuracy Comparisons with Baselines

This section evaluates FCDM’s performance by comparing it against 10 baselines on 3 datasets. We focus on evaluating the SSIM and PSNR metrics specifically within the masked regions rather than across the entire image, allowing us to precisely measure the model’s ability to inpaint the most challenging portions of the sinogram, where data is missing or corrupted. We also evaluate the images reconstructed by Gridrec(Dowd et al. 1999) on SSIM and PSNR.

Tab. 1 summarizes the performance of FCDM and baselines on the Real-world dataset. Fig. 3 shows the inpainted sinograms and reconstructed images using Gridrec at a mask ratio of 0.8, highlighting visual quality. Results show that FCDM significantly outperforms all baselines on the more complex Real-world dataset. The simplicity of the Shapes and Shepp2d datasets allows prior baselines to perform well, making our improvements relatively modest (but still clear) in those cases. The Real-world dataset poses greater challenges, where our model excels by leveraging sinogram-specific properties, yielding a clear and sub-

Methods	SSIM			PSNR		
	Mask Ratio			Mask Ratio		
	0.4	0.6	0.8	0.4	0.6	0.8
Ours	0.937	0.938	0.940	31.0	31.1	31.3
W/o FEME	0.916	0.918	0.919	29.3	29.5	29.6
W/o FANS	0.911	0.914	0.916	28.9	29.0	29.3

Table 4: **Ablation results on FEME and FANS.** Removing FEME reduces model performance, and without FANS leads to a decline in model performance either.

stantial advantage in inpainting quality over other methods.

4.3 Ablation Studies

Impact of Bidirectional Frequency Domain Convolutions

We first examine the impact of BFDC by comparing several convolutional configurations. We test the full model as well as variants using only spatial-domain convolutions, 2D frequency convolutions, and single-direction frequency convolutions along either the detector axis or projection angles. Results show that removing frequency-domain convolutions degrades performance, as spatial convolutions alone fail to disentangle overlapping sinogram features. While 2D frequency convolutions lack directional control and single-direction ones capture only partial spectral information, the BFDC approach performs best. We also compare peak memory, runtime, and FLOPs between FCDM with and without frequency-domain convolutions, showing no significant difference (see appendix).

Contribution of Tailored Loss Functions The second part of our ablation study examines the role of the tailored loss functions. We conduct experiments where the absorption consistency loss or the frequency domain loss is removed from the training process. Results in Tab. 3 demonstrate that the tailored losses are essential for achieving high-quality inpaintings.

Impact of Fourier-Enhanced Mask Embedding and Frequency-Adaptive Noise Scheduling

To assess the contribution of FEME, we compare models trained with and without FEME in Tab. 4. The model trained with a standard 0/1 binary mask exhibits a drop in performance. By contrast, the FEME-enhanced model consistently achieves higher SSIM and PSNR scores, demonstrating that incorporating projection angle information helps the model better infer missing regions by leveraging angular dependencies. Finally, we evaluate the impact of FANS by comparing two different noise injection strategies: standard Gaussian noise and our proposed FANS. As shown in Tab. 4, using standard Gaussian noise leads to lower SSIM and PSNR scores, as it does not account for the varying importance of different frequency components during the diffusion process. In contrast, our FANS improves performance by preserving low-frequency components in early steps to stabilize global structure recovery, and gradually emphasizing high-frequency details in later steps for fine reconstruction.

5 Conclusion

This work introduces FCDM, a new diffusion-based sinogram inpainting model that integrates bidirectional frequency-domain convolutions, physics-guided loss, Fourier-enhanced mask embedding, and frequency-adaptive noise scheduling. The evaluation results demonstrate that FCDM closely approximates the ground truth. Ablation studies further validate the effectiveness.

References

- Bicer, T.; Gürsoy, D.; Andrade, V. D.; Kettimuthu, R.; Scullin, W.; Carlo, F. D.; and Foster, I. T. 2017. Trace: a high-throughput tomographic reconstruction engine for large-scale datasets. *Advanced structural and chemical imaging*, 3: 1–10.
- Brenner, D. J.; and Hall, E. J. 2007. Computed tomography—an increasing source of radiation exposure. *New England journal of medicine*, 357(22): 2277–2284.
- Chambolle, A.; and Lions, P.-L. 1997. Image recovery via total variation minimization and related problems. *Numerische Mathematik*, 76: 167–188.
- Chen, P.; Wahib, M.; Takizawa, S.; Takano, R.; and Matsuo, S. 2019. IFDK: A scalable framework for instant high-resolution image reconstruction. In *Proceedings of the International Conference for High Performance Computing, Networking, Storage and Analysis*, 1–24.
- Chi, L.; Jiang, B.; and Mu, Y. 2020a. Fast Fourier Convolution. In Larochelle, H.; Ranzato, M.; Hadsell, R.; Balcan, M.; and Lin, H., eds., *Advances in Neural Information Processing Systems*, volume 33, 4479–4488. Curran Associates, Inc.
- Chi, L.; Jiang, B.; and Mu, Y. 2020b. Fast fourier convolution. *Advances in Neural Information Processing Systems*, 33: 4479–4488.
- Cooley, J. W.; and Tukey, J. W. 1965. An algorithm for the machine calculation of complex Fourier series. *Mathematics of computation*, 19(90): 297–301.
- De Andrade, V.; Deriy, A.; Wojcik, M. J.; Gürsoy, D.; Shu, D.; Fezzaa, K.; and De Carlo, F. 2016. Nanoscale 3D imaging at the Advanced Photon Source. *SPIE Newsroom*, 10: 006461.
- De Carlo, F.; Gürsoy, D.; Ching, D. J.; Batenburg, K. J.; Ludwig, W.; Mancini, L.; Marone, F.; Mokso, R.; Pelt, D. M.; Sijbers, J.; et al. 2018. TomoBank: a tomographic data repository for computational x-ray science. *Measurement Science and Technology*, 29(3): 034004.
- Defrise, M.; and Clack, R. 1994. A cone-beam reconstruction algorithm using shift-variant filtering and cone-beam backprojection. *IEEE transactions on medical imaging*, 13(1): 186–195.
- Deng, Y.; Hui, S.; Meng, R.; Zhou, S.; and Wang, J. 2022. Hourglass attention network for image inpainting. In *Euro-pean conference on computer vision*, 483–501. Springer.
- Dowd, B. A.; Campbell, G. H.; Marr, R. B.; Nagarkar, V. V.; Tipnis, S. V.; Axe, L.; and Siddons, D. P. 1999. Developments in synchrotron x-ray computed microtomography at the National Synchrotron Light Source. In *Developments in X-ray Tomography II*, volume 3772, 224–236. SPIE.
- Dyer, E. L.; Roncal, W. G.; Prasad, J. A.; Fernandes, H. L.; Gürsoy, D.; De Andrade, V.; Fezzaa, K.; Xiao, X.; Vogelstein, J. T.; Jacobsen, C.; et al. 2017. Quantifying mesoscale neuroanatomy using X-ray microtomography. *eneuro*, 4(5).
- Guo, J.; Lopez-Tapia, S.; and Katsaggelos, A. K. 2025. Advancing Limited-Angle CT Reconstruction Through Diffusion-Based Sinogram Completion. *arXiv preprint arXiv:2505.19385*.
- Gürsoy, D.; De Carlo, F.; Xiao, X.; and Jacobsen, C. 2014. TomoPy: a framework for the analysis of synchrotron tomographic data. *Journal of synchrotron radiation*, 21(5): 1188–1193.
- Herman, G. T.; and Meyer, L. B. 1993. Algebraic reconstruction techniques can be made computationally efficient (positron emission tomography application). *IEEE transactions on medical imaging*, 12(3): 600–609.
- Hidayetoğlu, M.; Bicer, T.; De Gonzalo, S. G.; Ren, B.; De Andrade, V.; Gürsoy, D.; Kettimuthu, R.; Foster, I. T.; and Wen-mei, W. H. 2020. Petascale XCT: 3D image reconstruction with hierarchical communications on multi-GPU nodes. In *SC20: International Conference for High Performance Computing, Networking, Storage and Analysis*, 1–13. IEEE.
- Hidayetoğlu, M.; Biçer, T.; De Gonzalo, S. G.; Ren, B.; Gürsoy, D.; Kettimuthu, R.; Foster, I. T.; and Hwu, W.-m. W. 2019. MemXCT: Memory-centric X-ray CT reconstruction with massive parallelization. In *Proceedings of the International Conference for High Performance Computing, Networking, Storage and Analysis*, 1–56.
- Ho, J.; Jain, A.; and Abbeel, P. 2020. Denoising diffusion probabilistic models. *Advances in neural information processing systems*, 33: 6840–6851.
- Hu, D.; Zhang, Y.; Quan, G.; Xiang, J.; Coatrieux, G.; Luo, S.; Coatrieux, J.-L.; Ji, X.; Han, H.; and Chen, Y. 2023. CROSS: Cross-domain residual-optimization-based structure strengthening reconstruction for limited-angle CT. *IEEE Transactions on Radiation and Plasma Medical Sciences*, 7(5): 521–531.
- Jiaze, E.; Liu, Z.; Bicer, T.; Banerjee, S.; Kettimuthu, R.; Ren, B.; and Foster, I. T. 2025. SinoTx: A Transformer-based Model for Sinogram Inpainting. *Electronic Imaging*, 37: 1–6.
- Kak, A. C.; and Slaney, M. 2001. *Principles of computerized tomographic imaging*. SIAM.
- Ko, K.; and Kim, C.-S. 2023. Continuously masked transformer for image inpainting. In *Proceedings of the IEEE/CVF International Conference on Computer Vision*, 13169–13178.
- Koroshetz, W.; Gordon, J.; Adams, A.; Beckel-Mitchener, A.; Churchill, J.; Farber, G.; Freund, M.; Gnadt, J.; Hsu, N. S.; Langhals, N.; et al. 2018. The state of the NIH BRAIN initiative. *Journal of Neuroscience*, 38(29): 6427–6438.
- Li, J.; Han, K.; Wang, P.; Liu, Y.; and Yuan, X. 2020. Anisotropic convolutional networks for 3d semantic scene

- completion. In *Proceedings of the IEEE/CVF Conference on Computer Vision and Pattern Recognition*, 3351–3359.
- Li, X.; Guo, Q.; Lin, D.; Li, P.; Feng, W.; and Wang, S. 2022. Misf: Multi-level interactive siamese filtering for high-fidelity image inpainting. In *Proceedings of the IEEE/CVF conference on computer vision and pattern recognition*, 1869–1878.
- Li, Z.; Cai, A.; Wang, L.; Zhang, W.; Tang, C.; Li, L.; Liang, N.; and Yan, B. 2019a. Promising Generative Adversarial Network Based Sinogram Inpainting Method for Ultra-Limited-Angle Computed Tomography Imaging. *Sensors*, 19(18).
- Li, Z.; Cai, A.; Wang, L.; Zhang, W.; Tang, C.; Li, L.; Liang, N.; and Yan, B. 2019b. Promising generative adversarial network based sinogram inpainting method for ultra-limited-angle computed tomography imaging. *Sensors*, 19(18): 3941.
- Li, Z.; Zhang, W.; Wang, L.; Cai, A.; Liang, N.; Yan, B.; and Li, L. 2019c. A sinogram inpainting method based on generative adversarial network for limited-angle computed tomography. In *15th International Meeting on Fully Three-Dimensional Image Reconstruction in Radiology and Nuclear Medicine*, volume 11072, 345–349. SPIE.
- Liu, H.; Wang, Y.; Qian, B.; Wang, M.; and Rui, Y. 2024. Structure Matters: Tackling the Semantic Discrepancy in Diffusion Models for Image Inpainting. In *Proceedings of the IEEE/CVF Conference on Computer Vision and Pattern Recognition*, 8038–8047.
- Liu, J.; Anirudh, R.; Thiagarajan, J. J.; He, S.; Mohan, K. A.; Kamilov, U. S.; and Kim, H. 2023. Dolce: A model-based probabilistic diffusion framework for limited-angle ct reconstruction. In *Proceedings of the IEEE/CVF international conference on computer vision*, 10498–10508.
- Lugmayr, A.; Danelljan, M.; Romero, A.; Yu, F.; Timofte, R.; and Van Gool, L. 2022. Repaint: Inpainting using denoising diffusion probabilistic models. In *Proceedings of the IEEE/CVF conference on computer vision and pattern recognition*, 11461–11471.
- Mohan, K. A.; Venkatakrishnan, S.; Gibbs, J. W.; Gulsoy, E. B.; Xiao, X.; De Graef, M.; Voorhees, P. W.; and Bouman, C. A. 2015. TIMBIR: A method for time-space reconstruction from interlaced views. *IEEE Transactions on Computational Imaging*, 1(2): 96–111.
- Müller, S.; Pietsch, P.; Brandt, B.-E.; Baade, P.; De Andrade, V.; De Carlo, F.; and Wood, V. 2018. Quantification and modeling of mechanical degradation in lithium-ion batteries based on nanoscale imaging. *Nature communications*, 9(1): 2340.
- Pelt, D. M.; and Batenburg, K. J. 2013. Fast tomographic reconstruction from limited data using artificial neural networks. *IEEE Transactions on Image Processing*, 22(12): 5238–5251.
- Radon, J. 1917. Über die Bestimmung von Funktionen durch ihre Integralwerte längs gewisser Mannigfaltigkeiten. *Berichte über die Verhandlungen der Sächsischen Akademie der Wissenschaften*, 69: 262–277. 00000.
- Rombach, R.; Blattmann, A.; Lorenz, D.; Esser, P.; and Ommer, B. 2022. High-resolution image synthesis with latent diffusion models. In *Proceedings of the IEEE/CVF conference on computer vision and pattern recognition*, 10684–10695.
- Satpathy, Y.; Nikitin, V.; Hana, J.; Venkatesan, K. R.; Tran, F.; Chen, S.; Shevchenko, P.; De Carlo, F.; Kettimuthu, R.; Zekriardehani, S.; Mapkar, J.; Krishnamurthy, A.; and Tekawade, A. 2024. Multiscale porosity characterization in additively manufactured polymer nanocomposites using micro-computed tomography. *Additive Manufacturing*, 86: 104199.
- Song, J.; Meng, C.; and Ermon, S. 2020. Denoising diffusion implicit models. *arXiv preprint arXiv:2010.02502*.
- Sun, Y.; Liu, J.; Xie, M.; Wohlberg, B.; and Kamilov, U. S. 2021. CoIL: Coordinate-Based Internal Learning for Tomographic Imaging. *IEEE Transactions on Computational Imaging*, 7: 1400–1412.
- Suvorov, R.; Logacheva, E.; Mashikhin, A.; Remizova, A.; Ashukha, A.; Silvestrov, A.; Kong, N.; Goka, H.; Park, K.; and Lempitsky, V. 2022. Resolution-robust large mask inpainting with fourier convolutions. In *Proceedings of the IEEE/CVF winter conference on applications of computer vision*, 2149–2159.
- Unser, M. 1999. Splines: A perfect fit for signal and image processing. *IEEE Signal processing magazine*, 16(6): 22–38.
- Valat, E.; Farrahi, K.; and Blumensath, T. 2023a. Sinogram Inpainting with Generative Adversarial Networks and Shape Priors. *Tomography*, 9(3): 1137–1152.
- Valat, E.; Farrahi, K.; and Blumensath, T. 2023b. Sinogram inpainting with generative adversarial networks and shape priors. *Tomography*, 9(3): 1137–1152.
- Van der Walt, S.; Schönberger, J. L.; Nunez-Iglesias, J.; Boulogne, F.; Warner, J. D.; Yager, N.; Goullart, E.; and Yu, T. 2014. scikit-image: image processing in Python. *PeerJ*, 2: e453.
- Wagner, F.; Thies, M.; Maul, N.; Pfaff, L.; Aust, O.; Pechmann, S.; Syben, C.; and Maier, A. 2023. Geometric Constraints Enable Self-Supervised Sinogram Inpainting in Sparse-View Tomography. *arXiv preprint arXiv:2302.06436*.
- Wang, Z.; Bovik, A. C.; Sheikh, H. R.; and Simoncelli, E. P. 2004. Image quality assessment: from error visibility to structural similarity. *IEEE transactions on image processing*, 13(4): 600–612.
- Würfl, T.; Ghesu, F. C.; Christlein, V.; and Maier, A. 2016. Deep learning computed tomography. In *International conference on medical image computing and computer-assisted intervention*, 432–440. Springer.
- Xie, E.; Ni, P.; Zhang, R.; and Li, X. 2022. Limited-angle ct reconstruction with generative adversarial network sinogram inpainting and unsupervised artifact removal. *Applied Sciences*, 12(12): 6268.
- Yao, L.; Lyu, Z.; Li, J.; and Chen, Q. 2024. No ground truth needed: unsupervised sinogram inpainting for nanoparticle

electron tomography (UsiNet) to correct missing wedges. *npj Computational Materials*, 10(1): 28.

Zhang, G.; Ji, J.; Zhang, Y.; Yu, M.; Jaakkola, T.; and Chang, S. 2023. Towards Coherent Image Inpainting Using Denoising Diffusion Implicit Models. *arXiv:2304.03322*.

Zhao, C.; Wang, C.; Liu, X.; Hwang, I.; Li, T.; Zhou, X.; Diao, J.; Deng, J.; Qin, Y.; Yang, Z.; et al. 2024. Suppressing strain propagation in ultrahigh-Ni cathodes during fast charging via epitaxial entropy-assisted coating. *Nature Energy*, 9(3): 345–356.

Zhao, J.; Chen, Z.; Zhang, L.; and Jin, X. 2018. Unsupervised learnable sinogram inpainting network (SIN) for limited angle CT reconstruction. *arXiv preprint arXiv:1811.03911*.

Appendix

A Design Rationales of Key Components

FCDM is composed of several interacting components, each designed to address a specific aspect of the sinogram inpainting challenge. While the main paper has already discussed the motivations, this section provides further clarification on the reasoning behind their structural choices or usage contexts.

A.1 Bidirectional Frequency-Domain Convolution in Latent Space

A central design choice in FCDM is the placement of the bidirectional frequency-domain convolution (FreqConv): whether it should operate directly on the input sinogram or on the latent representation produced by the encoder. While applying FreqConv at the input level may seem attractive due to access to full-resolution data, we argue that performing it in the latent space is both intuitively and functionally more appropriate for our task.

Sinogram data, particularly from real-world sources, contain a significant amount of noise and physically irrelevant high-frequency components. Applying frequency-domain filtering directly to this raw input risks amplifying these artifacts and misinterpreting noise as structural signal. In contrast, the encoder in FCDM is trained not merely to reduce spatial dimensions, but to abstract physically meaningful features while suppressing noise and redundancy. The resulting latent space provides a cleaner, semantically richer representation of the underlying projection structure.

This design choice aligns with established practices in modern generative models and vision transformers, where attention or frequency-based operations are often applied at the feature level rather than on raw-resolution input (Suvorov et al. 2022; Chi, Jiang, and Mu 2020b), allowing better generalization and noise robustness.

Theoretical Complexity Analysis We briefly compare the theoretical complexity of applying FreqConv at different stages of the model pipeline. In the first setting, FreqConv is applied directly on the input sinogram of size $C \times H \times W$, followed by an encoder. In the second setting, the encoder first maps the input into a latent feature space of size $C_L \times H_L \times W_L$, after which FreqConv is applied.

In the input-level setting, the dominant operations include the forward and inverse Fourier transforms and the element-wise multiplication in the frequency domain, followed by spatial convolution and the standard encoder. The corresponding total complexity can be approximated as:

$$\mathcal{O}(C \cdot HW \cdot \log HW + C^2 k^2 HW) \quad (13)$$

Here, k denotes the spatial kernel size used in the convolution operations.

In the latent-level setting, the encoder is applied first, and FreqConv is performed on its output. The overall complexity then becomes:

$$\mathcal{O}(C^2 k^2 HW + C_L \cdot \frac{HW}{r^2} \cdot \log \frac{HW}{r^2} + C_L^2 k^2 \frac{HW}{r^2}) \quad (14)$$

Variant	SSIM	PSNR	Mem	Time	FLOPs
@Input	0.948	32.5	3.7	0.37	18.7
@Latent	0.955	33.1	3.7	0.36	18.5
W/o	0.894	28.3	3.6	0.33	18.5

Table 5: **Performance comparison between input-level, latent-level, and without FreqConv.** Results are reported under AutoEncoder-only inference and measured on the Real-world dataset using batch size 1. Memory is measured in gigabytes (GB), time in seconds (s), and FLOPs in gigaflops (G).

Here, r denotes the effective downsampling ratio of the encoder, and we assume that both versions use the same encoder architecture. While the encoder cost is present in both settings, the frequency-related operations are significantly reduced in the latent case due to the smaller spatial resolution and potentially lower channel dimensionality. These expressions suggest that placing FreqConv in the latent space is computationally advantageous, particularly when working with high-resolution inputs.

AutoEncoder-Level Performance Analysis To further assess the practical impact of FreqConv placement, we compare the runtime efficiency and inpainting quality of two AutoEncoder variants: one applying FreqConv directly on the input sinogram (input-level), and the other applying it on the encoded latent features (latent-level). This analysis isolates the AutoEncoder module from the full model, excluding any diffusion-based refinement or masking strategies, and focuses solely on the encoder-decoder backbone.

All experiments are conducted in inference using the same implementation setup as the main paper, with batch size set to 1 to reflect standard deployment settings. We enable common performance optimizations, including `torch.compile()` for graph-mode execution, `torch.autocast()` for mixed-precision (fp16) inference, and `cudnn.benchmark = True` for automatic kernel selection. All evaluations are performed on the Real-world dataset.

In addition to the two placement variants, we also include an ablation setting where the entire FreqConv module is removed, reducing the encoder-decoder to a purely spatial baseline. As shown in Tab. 5, the latent-level variant achieves slightly higher inpainting quality in both SSIM and PSNR, while also reducing maximum allocated memory, inference time, and FLOPs compared to input-level placement. The baseline without FreqConv exhibits the lowest computational footprint but suffers from a small drop in inpainting accuracy. These results support our decision to retain FreqConv processing, and to place it in the latent space, where it achieves a favorable balance between effectiveness and efficiency.

BFDC Configuration	SSIM	PSNR
Original	0.955	33.1
Isotropic	0.941	31.7
Angular-dominant	0.936	31.2

Table 6: **Impact of BFDC axis weighting on AutoEncoder performance.** Results are reported under AutoEncoder-only inference using the Real-world dataset with a mask ratio of 0.8.

A.2 Absorption Consistency via Inverse Radon

Our proposed physics-guided loss contains a total absorption consistency term, referred to as L_{absorp} , which enforces the principle that the cumulative attenuation along each X-ray path should remain stable across the projection domain. This principle reflects a fundamental property of X-ray imaging: the amount of total energy absorbed by a scanned object should be preserved globally.

To implement this constraint, we apply an inverse Radon transform to the predicted sinogram, producing an approximate attenuation map. Although the formulation uses analytic operations rather than full physical modeling, it approximates a domain-consistent property rooted in imaging physics. The inverse Radon transform used here is not intended as an accurate simulation of material attenuation, but rather as a differentiable surrogate that allows the network to reason about global attenuation structure.

This design reflects a broader philosophy of physics-guided learning: rather than modeling the full measurement process, we incorporate physics-motivated constraints into the loss function, using approximate but structured operations to inform optimization.

B Supplementary Implementation Details

Hyperparameter Design and Sensitivity Our BFDC module applies axis-specific weighting to frequency components along the projection angle (W) and detector (H) dimensions. This is controlled by three hyperparameters: a_s , the weight for spatial convolution; a_w , the weight for angular (row-wise) convolution; and a_h , the weight for detector (column-wise) convolution. In our main experiments, we set $\alpha_h = 0.55$ and $\alpha_w = 0.45$, based on the observation that sinograms typically exhibit smoother variation along the angular direction but more complex high-frequency structure along the detector axis.

To evaluate the impact of directional weighting within BFDC, we conduct an ablation study in the context of the AutoEncoder module only. All experiments are performed on the Real-world dataset with a mask ratio of 0.8. We compare our settings in the main paper with two configurations: a balanced isotropic setting ($\alpha_h = \alpha_w = 0.5$), and an angular-dominant setting ($\alpha_h = 0.45$, $\alpha_w = 0.55$). Other implementations are identical to those in the main paper.

The results in Tab. 6 show that both isotropic and angular-dominant lead to a consistent drop in inpainting as measured by SSIM and PSNR. In particular, treating the two axes equally or overemphasizing the angular direction causes

FANS Configuration	SSIM	PSNR
Original	0.940	31.3
Aggressive	0.931	30.5
W/o FANS	0.916	29.3

Table 7: **Ablation study of FANS parameters.** Results are reported on the Real-world dataset with a mask ratio of 0.8.

λ	SSIM	PSNR
0.0 (no constraint)	0.933	30.6
0.3 (default)	0.940	31.3
1.0 (hard constraint)	0.929	30.2

Table 8: **Impact of the soft absorption constraint.** A moderate value of λ achieves the best balance between enforcing projection-level consistency and maintaining model generalization.

both metrics to decline, suggesting that directional decomposition is not merely a tuning artifact but a meaningful inductive bias. These results confirm the relevance of axis-aware frequency weighting in our design.

FANS introduces a frequency-adaptive modulation of Gaussian noise in the diffusion process, aiming to align noise injection with the structural properties of sinograms. This modulation is controlled by two hyperparameters: α , which determines the emphasis applied to high-frequency components, and β , which controls the maximum contribution from low-frequency noise.

We set $\alpha = 1.1$ and $\beta = 0.8$, which offers a balance between spectral selectivity and model stability. If either parameter is set too low, the frequency-adaptive behavior becomes negligible and FANS degenerates to a standard uniform noise schedule. On the other hand, setting either too high can lead to excessive perturbation, destabilizing the denoising trajectory or disrupting structural integrity. We found β to be particularly sensitive: since it controls low-frequency disturbance, large values can degrade the global consistency of the projection space and introduce instability in the inpainted sinograms. Therefore, we adopt a slightly lower value for β , ensuring that FANS remains conservative in how it perturbs foundational structure.

To validate the impact of FANS and the sensitivity to its hyperparameters, we compare a more aggressive variant ($\alpha = 1.5$, $\beta = 1.2$) with stronger frequency bias on the Real-world dataset under a mask ratio of 0.8. Other implementations are identical to those in the main paper.

As shown in Tab. 7, the default FANS configuration achieves the highest SSIM and PSNR, indicating that frequency-aware noise modulation helps improve inpainting quality. The one without FANS performs worse, as it lacks any spectral adaptation. The over-biased variant shows a noticeable drop in both metrics, confirming that excessive perturbation of either frequency band can destabilize the reconstruction process.

To promote projection-level consistency, we introduce a soft absorption constraint that penalizes deviations in row-wise attenuation in FANS. The strength of this constraint is controlled by a hyperparameter λ , which balances physical regularization and model flexibility. Large values of λ can over-constrain the denoising process and degrade generalization, while small values render the constraint ineffective. To validate the impact of λ , we compare our default setting with two other variants—no constraint ($\lambda = 0.0$) and hard constraint ($\lambda = 1.0$)—on the Real-world dataset under a mask ratio of 0.8. Other implementations are identical to those in the main paper. As shown in Tab. 8, the default setting achieves the best inpainting results.

Dataset As described in the main paper, we use three datasets in our experiments: Real-world, Shape, and Shepp2d. All data undergo a consistent preprocessing pipeline, including ring artifact removal, rotation center alignment, and intensity normalization to the $[0,1]$ range. For real-world scans, we follow the official guidelines provided by the TomoPy library (Gürsoy et al. 2014). For parameters such as projection counts, rotation centers, and angular sampling are adjusted based on the information provided by TomoBank (De Carlo et al. 2018).

Real-world dataset (De Carlo et al. 2018) consists of real sinogram images obtained from various materials and objects. It includes samples with dynamic features (Mohan et al. 2015) and in situ (Pelt and Batenburg 2013) measurements, which captures wide-range of experiments at APS and other synchrotron facilities. This dataset, provided by the X-ray tomography data bank, includes a range of noise levels and artifacts that are typical in real-world settings, making it significantly more complex than simulated and synthetic datasets. This complexity offers a rigorous test of the model’s robustness and ability to handle practical challenges in sinogram inpainting.

Shape dataset generated using the scikit-image library (Van der Walt et al. 2014) contains a variety of simulated geometric shapes, including circles, rectangles, and triangles. This dataset introduces a range of geometric complexities, allowing us to assess the model’s ability to reconstruct shapes with sharp edges and varying curvature.

Shepp2d dataset generated by the Tomopy library (Gürsoy et al. 2014) comprises simulated shepp-logan phantoms, offering a controlled environment for evaluating the accuracy and stability of inpainting algorithms. These phantoms are less complex and ideal for testing basic inpainting capabilities.

Metrics As described in the main paper, we evaluate inpainting quality using SSIM and PSNR. All images are normalized to the $[0, 1]$ range before metric computation. SSIM is computed in single-scale mode using a 11×11 Gaussian kernel ($\sigma = 1.5$), following the original formulation. All metrics are computed on grayscale images.

Mask Type	SSIM	PSNR
Block	0.941	31.1
Stripe	0.938	31.3

Table 9: **Inpainting robustness under different mask patterns.** All experiments are conducted on the Real-world dataset with a mask ratio of 0.8.

Methods	Mem	Time
Ours	5.2	0.60
RePaint	5.5	1.44
CoPaint	5.1	1.03
StrDiffusion	5.0	0.72
LaMa	2.5	0.11

Table 10: **Inference efficiency comparison with representative baselines under identical settings.** Memory is measured in gigabytes (GB), and time in seconds (s).

C Supplementary Evaluation Results

C.1 Evaluation Results for Other Datasets

11, 12, and 4 present the quantitative and qualitative comparisons on the Shape and Shepp2d datasets against several state-of-the-art baselines. All implementations are identical to those in the main paper. For both datasets, FCDM consistently achieves higher SSIM and PSNR scores compared to previous baselines, indicating superior inpainting accuracy of our model.

On the Shape dataset, which consists of geometric shapes with distinct edges and simple textures, our model demonstrates strong performance in accurately completing sinograms of objects with sharp boundary features. For the Shepp2d dataset, despite its simpler structure, the results confirm that our model can still effectively capture its features and maintain high-quality inpainting. Although the improvements in these controlled datasets are relatively modest, they showcase our model’s robustness and consistency in diverse scenarios, demonstrating that it can perform on par with or better than previous baselines.

C.2 Robustness to Different Mask Types

We evaluate the robustness of our model across diverse occlusion patterns by applying two other types of masks to the Real-world dataset, each with a fixed missing ratio of 0.8: (1) block-wise occlusion, where large contiguous regions are missing; and (2) structured stripe masks with regularly spaced missing columns. Other implementations are identical to those in the main paper.

As shown in Tab. 9, the model maintains stable inpainting performance across all settings. This suggests that the proposed method generalizes well to different occlusion geometries without requiring mask-specific adaptation.

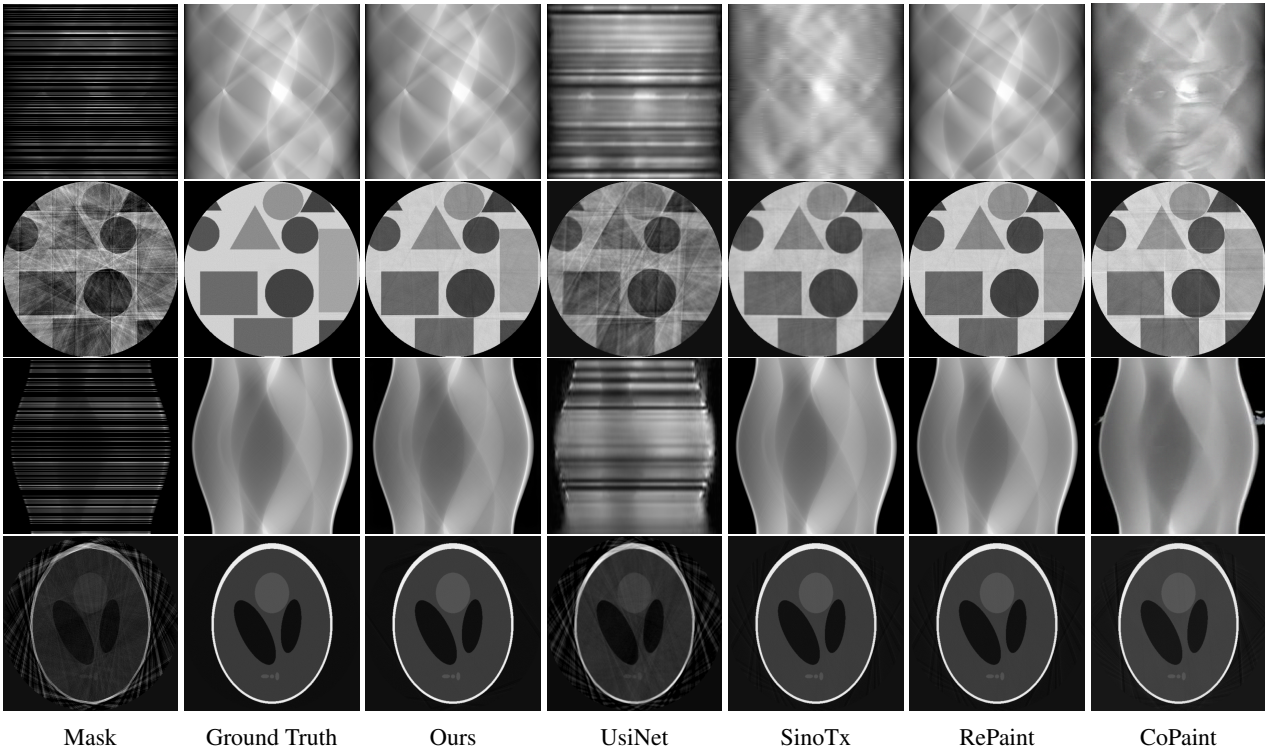


Figure 4: **Visual results of Shape and Shepp2d datasets.** Line 1 and 3 are visual results of sinogram inpainting of Shape dataset and Shepp2d dataset, respectively. Line 2 and 4 are visual results of the reconstructed images of the sinograms using iRadon. The visual comparisons highlight our model’s ability to preserve structural details and reduce artifacts.

C.3 System Efficiency Comparison with Representative Baselines

To assess the practical deployment cost of FCDM, we compare its system efficiency of inference with several representative inpainting baselines, including both diffusion-based and convolution-based approaches. We report inference time and peak memory usage under identical experimental settings to ensure fair benchmarking. All implementations adopt PyTorch’s built-in graph and kernel optimizations: `torch.compile()` for graph-mode execution, `torch.autocast()` for mixed-precision inference (fp16), and `cudnn.benchmark = True` for dynamic kernel selection. All diffusion-based models use DDIM sampling (Song, Meng, and Ermon 2020) with 50 steps, and are evaluated on the Real-world dataset with mask ratio as 0.8, input resolution as 512×512 , and batch size as 1.

As shown in Tab. 10, despite incorporating frequency-aware modules, angular-aware masking, and physics-consistent constraints, FCDM maintains modest memory usage and inference time, comparable to or better than most existing diffusion models. While feedforward methods such as LaMa achieve faster inference, they suffer from significantly reduced reconstruction accuracy, underscoring the favorable accuracy-efficiency balance of our approach.

D Limitations

While FCDM demonstrates strong performance across diverse sinogram inpainting scenarios, it still has several limitations. First, our model assumes that each projection view contains valid information across the full detector span. In extreme cases where entire vertical stripes (i.e., detector regions) are missing across all angles, recovery may fail to produce plausible completions. Second, FCDM is trained under the assumption of monotonically ordered and unique projection angles. When the projection angles are shuffled, non-uniformly spaced, or duplicated, performance may degrade due to disrupted angular context. Third, as a generative model, FCDM may in rare cases hallucinate plausible but physically incorrect structures, particularly under extreme undersampling or ambiguous contexts. While our physics-guided losses aim to reduce such risks, addressing the broader issue of hallucination or inverse hallucination remains an important direction for future work, especially for safety-critical domains such as medical imaging.

Methods	SSIM			PSNR		
	Mask Ratio			Mask Ratio		
	0.4	0.6	0.8	0.4	0.6	0.8
Ours	0.956 (0.934)	0.958 (0.938)	0.960 (0.945)	35.3 (33.4)	35.4 (33.5)	35.7 (33.9)
RePaint	0.955 (0.934)	0.957 (0.937)	0.956 (0.939)	34.1 (33.3)	34.5 (33.7)	34.9 (33.7)
CoPaint	0.933 (0.915)	0.939 (0.919)	0.938 (0.916)	33.2 (31.6)	33.0 (31.3)	33.3 (31.3)
MISF	0.923 (0.908)	0.927 (0.905)	0.930 (0.911)	32.2 (30.1)	32.7 (30.3)	33.1 (30.8)
LaMa	0.912 (0.891)	0.918 (0.895)	0.919 (0.895)	31.5 (29.1)	31.2 (29.0)	31.7 (29.3)
StrDiffusion	0.884 (0.867)	0.887 (0.866)	0.890 (0.872)	28.3 (26.1)	28.5 (26.5)	28.9 (26.5)
SionTx	0.886 (0.867)	0.888 (0.869)	0.891 (0.870)	28.5 (26.1)	28.9 (26.5)	29.0 (27.1)
Hourglass	0.857 (0.832)	0.858 (0.831)	0.860 (0.839)	27.1 (24.7)	27.5 (24.3)	28.2 (26.5)
UsiNet	0.701 (0.680)	0.703 (0.681)	0.706 (0.682)	23.1 (21.9)	23.7 (21.9)	24.0 (22.3)
CoIL	0.836 (0.813)	0.836 (0.819)	0.839 (0.816)	25.9 (23.3)	26.1 (23.7)	26.3 (24.1)
CMT	0.824 (0.803)	0.829 (0.807)	0.827 (0.805)	23.9 (21.1)	24.0 (22.4)	24.2 (22.1)

Table 11: **Quantitative accuracy results on the Shape dataset.** The results demonstrate that our model excels in handling sinograms of objects with sharp edges and geometric structures, outperforming the baselines in the inpainting performance.

Methods	SSIM			PSNR		
	Mask Ratio			Mask Ratio		
	0.4	0.6	0.8	0.4	0.6	0.8
Ours	0.965 (0.937)	0.979 (0.955)	0.978 (0.962)	37.8 (36.7)	37.3 (36.9)	37.9 (35.6)
RePaint	0.962 (0.937)	0.964 (0.944)	0.977 (0.953)	37.2 (35.3)	37.5 (35.2)	37.4 (35.5)
CoPaint	0.942 (0.922)	0.947 (0.925)	0.946 (0.924)	35.0 (33.7)	35.8 (33.5)	36.0 (33.8)
MISF	0.932 (0.912)	0.939 (0.916)	0.939 (0.914)	33.5 (30.2)	33.3 (30.8)	33.8 (31.5)
LaMa	0.921 (0.898)	0.924 (0.901)	0.927 (0.903)	33.2 (31.0)	33.9 (31.4)	34.1 (31.9)
StrDiffusion	0.906 (0.887)	0.908 (0.888)	0.910 (0.893)	31.5 (29.5)	31.8 (29.9)	32.0 (30.3)
SionTx	0.967 (0.938)	0.968 (0.946)	0.970 (0.956)	37.2 (35.8)	37.3 (35.4)	37.5 (35.9)
Hourglass	0.882 (0.860)	0.886 (0.863)	0.891 (0.868)	28.5 (26.9)	28.7 (26.3)	28.9 (26.8)
UsiNet	0.714 (0.697)	0.719 (0.699)	0.722 (0.702)	23.1 (21.1)	23.0 (21.2)	23.6 (21.5)
CoIL	0.854 (0.839)	0.858 (0.840)	0.860 (0.849)	25.9 (23.8)	26.1 (24.0)	26.4 (24.8)
CMT	0.844 (0.827)	0.847 (0.827)	0.848 (0.827)	25.8 (23.3)	25.7 (23.3)	25.7 (23.5)

Table 12: **Quantitative accuracy results on the Shape2d dataset.** The controlled and simplified nature of the Shepp2d dataset enables previous baselines to perform well, yet our model still demonstrates clear improvements in the inpainting performance.